

PAPER

Mechanical writing of in-plane ferroelectric vortices by tip-force and their coupled chirality

To cite this article: L L Ma *et al* 2020 *J. Phys.: Condens. Matter* **32** 035402

View the [article online](#) for updates and enhancements.



IOP | ebooks™

Bringing together innovative digital publishing with leading authors from the global scientific community.

Start exploring the collection—download the first chapter of every title for free.

Mechanical writing of in-plane ferroelectric vortices by tip-force and their coupled chirality

L L Ma^{2,3}, W J Chen^{1,2,3,4} , Biao Wang², W M Xiong^{2,3} and Yue Zheng^{2,3}

¹ School of Materials, Sun Yat-sen University, 510275 Guangzhou, People's Republic of China

² State Key Laboratory of Optoelectronic Materials and Technologies, School of Physics, Sun Yat-sen University, 510275 Guangzhou, People's Republic of China

³ Micro and Nano Physics and Mechanics Research Laboratory, School of Physics, Sun Yat-sen University, 510275 Guangzhou, People's Republic of China

E-mail: chenweijin@mail.sysu.edu.cn (W J Chen)

Received 16 July 2019, revised 30 August 2019

Accepted for publication 26 September 2019


Published 23 October 2019



Abstract

Recent experiments have demonstrated the existence of vortex or flux-closure domains in ferroelectric nanostructures, which are attractive to develop high-density data storage and novel configurable electronic devices. However, it remains challenging to stabilize in-plane vortex or flux-closure domains in ferroelectric film for the absence of a lateral geometry confinement. Based on a 3D phase field model, here we show that stabilization of isolated or interacting in-plane vortices in ferroelectric film can be achieved via applying a mechanical tip-force. The formation of such dipole vortices is caused by a conjoint effect of the tip-force-induced depolarization effect and in-plane strain. The effects of factors like film thickness, misfit strain, tip force and temperature on the vortex formation are systematically revealed and summarized as phase diagrams. The interaction between tip-induced vortices is also investigated. It is found that as the two tips get closer than the critical distance, the two initially isolated vortices become coupled, with identical or opposite chirality, depending on the distance between the two tips. A maximum data storage density of isolated in-plane vortices in ferroelectric thin film is estimated to be $\sim 1 \text{ Tb in}^{-2}$. Our work thus demonstrates a mechanical strategy to stabilize dipole vortices, and provides a comprehensive insight into the characteristics of ferroelectric film under a mechanical tip force.

Keywords: ferroelectric, vortex, domain structure, mechanical force, flexoelectricity

 Supplementary material for this article is available [online](#)

(Some figures may appear in colour only in the online journal)

1. Introduction

Ferroelectrics have attracted intensive academic and industry interests due to their outstanding functionalities and the great potentials in developing sensors, actuators and memories [1]. Ferroelectric domains and domain walls are exploited as the configurable electronic device elements such as memory cells [2, 3], diodes [4], and field transistors [5], and are promising

to enable high integration density and multifunctionalities [6, 7]. Particularly, as a novel kind of polarization pattern, flux-closure domains or continuous ferroelectric vortex are promising candidates in developing high density data storage and novel configurable electronic devices owing to their small size, strong stability and novel characteristics under different external stimuli [8, 9]. In fact, ferroelectric vortex, in analogy to magnetic vortex and skyrmion, is one typical kind of topological defects with a flux-closure of dipoles. They have drawn enormous attention in both theoretical and

⁴ Author to whom correspondence should be addressed.

experimental aspects after the prediction made around 2004 by first-principle-based simulations [8].

The existence of ferroelectric vortex or flux-closure domains has been reported in several ferroelectric nanostructures. For instance, long-range vortex arrays and flux-closure domains have been observed in $\text{PbTiO}_3/\text{SrTiO}_3$ superlattices [10, 11]. In BiFeO_3 film, vortex-like patterns have also been observed near the rhombohedral-orthorhombic morphotropic phase boundary (MPB) [12]. At the same time, experimental efforts were made to identify isolated ferroelectric vortices in nanodots [13, 14]. For the perspective of application, the control of vortex evolution and understanding their characteristics is essential and has also been intensively explored by theorists. Electrical methods, such as curled electric field, static fields and sweeping tip-field, have been exploited to switch the vortex chirality or induce vortex-polar transformation [15–17]. Mechanical strategies, for example, via applying strain, stress and torsion, have also been proven to enable multiplication, annihilation and chirality switching of ferroelectric vortex [18–20]. Geometry design, which can break the symmetry of the vortex system [21, 22] or induce coupling between polar and toroidal orders [23], is also feasible in controlling vortex chirality. Moreover, ferroelectric vortices have been reported to carry enhanced conductivity and negative dielectricity at the vortex core region (which can be regarded as a 1D domain wall) [24, 25]. All these endow a wonderful possibility of utilizing ferroelectric vortices in emerging electronic technologies.

Despite of the above mentioned advances, the stabilization of an isolated vortex or flux-closure domains in a continuous ferroelectric film remains challenging (usually, vortex arrays tend to form). This largely limits the practical applications of such dipole states in developing nanoscale devices like memory based on manipulation of a single vortex. The difficulty of forming isolated vortex or flux-closure domains in ferroelectric films is due to the lacking of lateral geometry confinement which provides a topological protection of the vortex dipole state. To form isolated vortex or flux-closure domains in ferroelectric films, other mechanisms rather than the geometry confinement must be pursued to provide the topological protection. It is noteworthy that recent works have shown that vortex and antivortex can be artificially generated in BiFeO_3 films via the use of a local tip electric field [24, 26, 27]. Meanwhile, mechanical tip-force has also been proved to be an attractive way to manipulate ferroelectric out-of-plane polarization [28–30], and magnetic skyrmions were reported to be induced by nonuniform strain similar to that caused by tip-force [31]. However, the tip-force effects on in-plane polarization texture is still poorly known, and the feasibility of writing isolated ferroelectric vortices by tip-force in ferroelectric films via a mechanical tip force remains unproved.

In this work, by performing three dimensional (3D) phase-field simulations, we report that the mechanical tip force can bring a conjoint effect of the tip-force-induced depolarization effect and in-plane strain, and consequently leads to the formation of isolated in-plane ferroelectric vortex in flat BaTiO_3 (BTO) thin films, as depicted in figure 1(a). The tip-force effects on in-plane polarization texture of the BTO thin

films are revealed. Then we calculate the phase diagrams of tip-force-induced vortex for various conditions, such as film thickness, misfit strain, tip force and temperature. Afterwards, the interaction between two tip-induced vortices is further simulated. An interesting chirality coupling behavior as a function of tip distance is discovered (see figure 1(b)). Our work thus demonstrates a mechanical strategy to stabilize isolated or interacting dipole vortices in ferroelectric film, and provides a comprehensive insight into the in-plane polarization characteristics of ferroelectric film under a mechanical tip force.

2. Simulation model and methods

In our phase-field model, we choose the spontaneous polarization field $\mathbf{P} = (P_1, P_2, P_3)$ as order parameter to characterize the domain structure of the BTO films. The time-dependent Ginzburg–Landau (TDGL) equations are employed to describe the temporal evolution of polarization field, i.e. $\partial P_i / \partial t = -M \delta F / \delta P_i$. Here M is the kinetic coefficient, t is time and F is the total free energy of the BTO film. The total free energy is expressed as $F = \iiint [f_{\text{Land}} + f_{\text{grad}} + f_{\text{elec}} + f_{\text{elas}} + f_{\text{flexo}}] dV + \iint f_{\text{surf}} dS$, where f_{Land} , f_{grad} , f_{elec} , f_{elas} and f_{surf} corresponds to the energy densities of bulk Landau energy, gradient energy, electrostatic energy, elastic energy and surface energy, respectively. Considering the large strain gradient induced by the tip-force, a flexoelectric coupling energy density $f_{\text{flexo}} = -\frac{1}{2} f_{ijkl} (P_k \varepsilon_{ij,l} - \varepsilon_{ij} P_{k,l})$ is included [32], with f_{ijkl} being the flexoelectric coupling coefficients. Accordingly, the flexoelectricity-modified polarization boundary condition is adopted at the top surface and bottom interface of film [33]. The Landau energy density takes the form of an eighth-order polynomial [34], $f_{\text{Land}} = a_1 \sum_i P_i^2 + a_{11} \sum_i P_i^4 + a_{12} \sum_{i>j} P_i^2 P_j^2 + a_{111} \sum_i P_i^6 + a_{112} \sum_{i \neq j} P_i^4 P_j^2 + a_{123} \prod_i P_i^2 + a_{1111} \sum_i P_i^8 + a_{1112} \sum_{i \neq j} P_i^6 P_j^2 + a_{1122} \sum_{i>j} P_i^4 P_j^4 + a_{1123} \sum_{i \neq j \neq k, j>k} P_i^4 P_j^2 P_k^2$, where a_i , a_{ij} , a_{ijk} , and a_{ijkl} are the thermodynamic coefficients, with integers i and j ranging from 1 to 3. The gradient energy density is described as $f_{\text{grad}} = \frac{1}{2} g_{ijkl} P_{i,j} P_{k,l}$ with g_{ijkl} being the gradient energy coefficients. The electrostatic energy density takes the form, $f_{\text{elec}} = -P_i E_i - \frac{1}{2} \varepsilon_b E_i E_i$, where ε_b is the background dielectric constant [35]. By including the effect of the eigen-strain $\varepsilon_{ij}^0 = Q_{ijkl} P_k P_l$ due to electrostriction, the elastic energy density can be expressed as $f_{\text{elas}} = \frac{1}{2} C_{ijkl} (\varepsilon_{ij} - \varepsilon_{ij}^0) (\varepsilon_{kl} - \varepsilon_{kl}^0)$ with C_{ijkl} and Q_{ijkl} being the elastic stiffness and electrostrictive tensor, respectively. The surface energy density is also considered to describe the lattice relaxation near the film surface [36], which is $f_{\text{surf}}(P_i) = \frac{D_1^s P_1^2}{2\delta_1^{\text{eff}}} + \frac{D_2^s P_2^2}{2\delta_2^{\text{eff}}} + \frac{D_3^s P_3^2}{2\delta_3^{\text{eff}}}$ with δ_i^{eff} being the extrapolation lengths, and D_i^s being the coefficients related to g_{ijkl} and surface orientation.

At each time instant of the polarization field evolution, the electric field and strain field are updated according to the temporary dipole configuration. The electric field is obtained by solving the electrostatic equilibrium equation $\nabla \cdot \mathbf{D} = 0$ under ideal short-circuit (SC) boundary condition, where \mathbf{D} is the electric

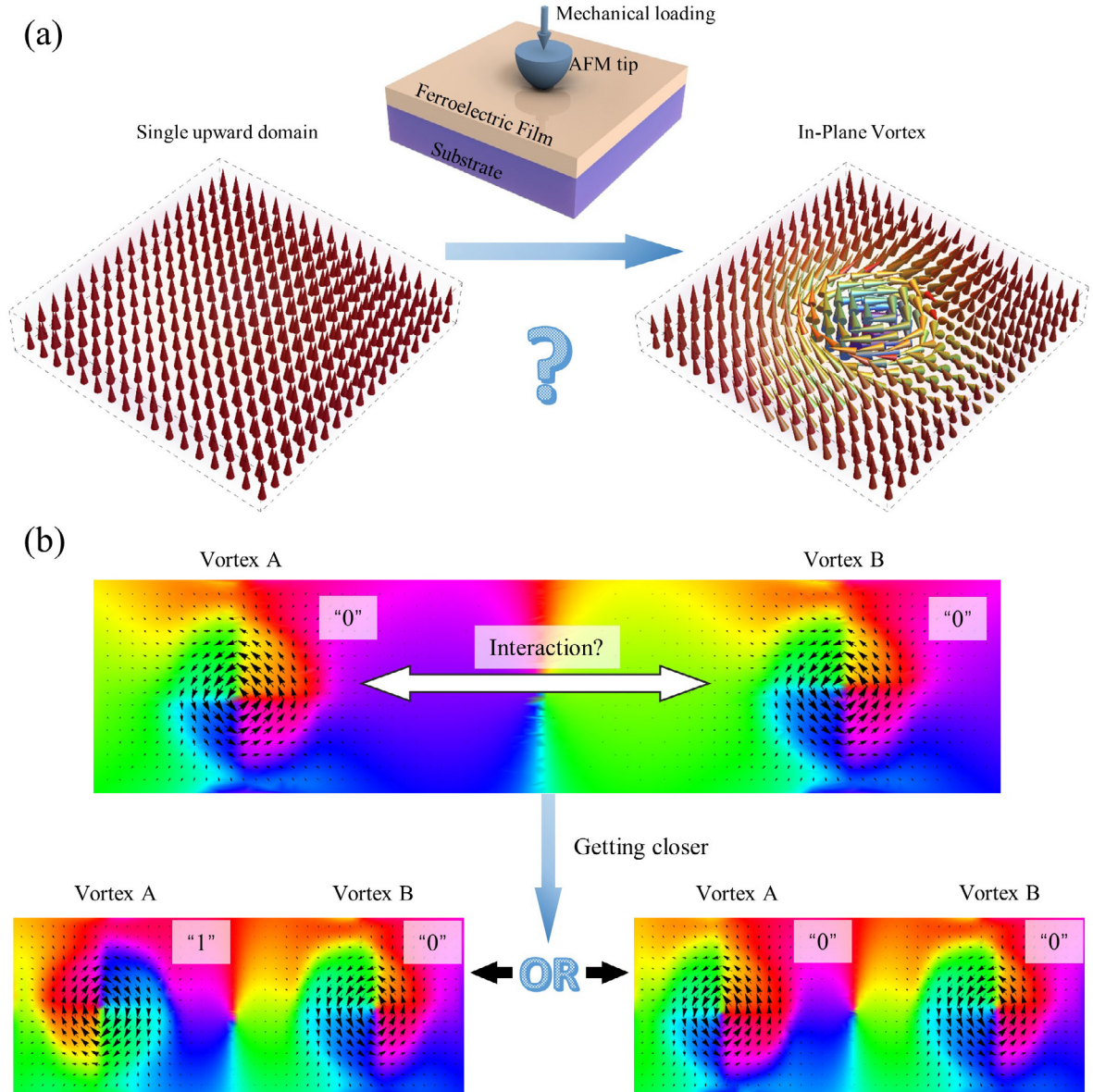


Figure 1. (a) Schematic illustrating the idea of using an AFM tip-force to induce in-plane dipole vortex in a ferroelectric film. (b) Schematic illustrating the possible coupling of chirality of two tip-induced vortices when the two tips are close to each other, with ‘0’ representing anti-clockwise and ‘1’ clockwise, respectively.

displacement. The strain field is obtained by solving the mechanical equilibrium equation $\nabla \cdot \sigma = 0$ under the stress boundary conditions along the out-of-plane direction exerted by the tip-force and the substrate, where σ is the stress tensor. Specifically, the BTO film is modeled to be (001) epitaxially grown on a deformable cubic substrate with a compressive in-plane misfit strain. For simplicity, the elastic stiffness coefficients of the substrate are taken to be those of BTO. The thickness of the substrate is assumed to be much thicker than that of BTO film. The stress boundary conditions exerted by the tip force at the bottom and top surfaces of the BTO film are extracted from finite element calculation of the tip-film contact problem [30], with the tip being made of Pt and having a radius of 50 nm (see supplementary figure S1 (stacks.iop.org/JPhysCM/32/035402/mmedia)). To

balance the accuracy and efficiency in calculating the strain/stress fields, in the finite element calculation, the thickness of the substrate layer in the simulation cell is taken to be 36Δ , and the bottom surface of the substrate is fixed in displacement. The periodic boundary conditions are adopted along the in-plane x and y directions for all calculations. The TDGL equations are solved by finite difference method, while the electrostatic and mechanical equilibrium equations are solved by the fast Fourier transform (FFT) technique. In the phase-field simulations, the mesh grid of the simulation film region is chosen as $128\Delta \times 128\Delta \times n_z\Delta$ with the grid space Δ being 0.4 nm for the first part of simulations (section 3.1) or 1 nm for the first part of simulations (section 3.2). All the parameters are same as those of previous work [30].

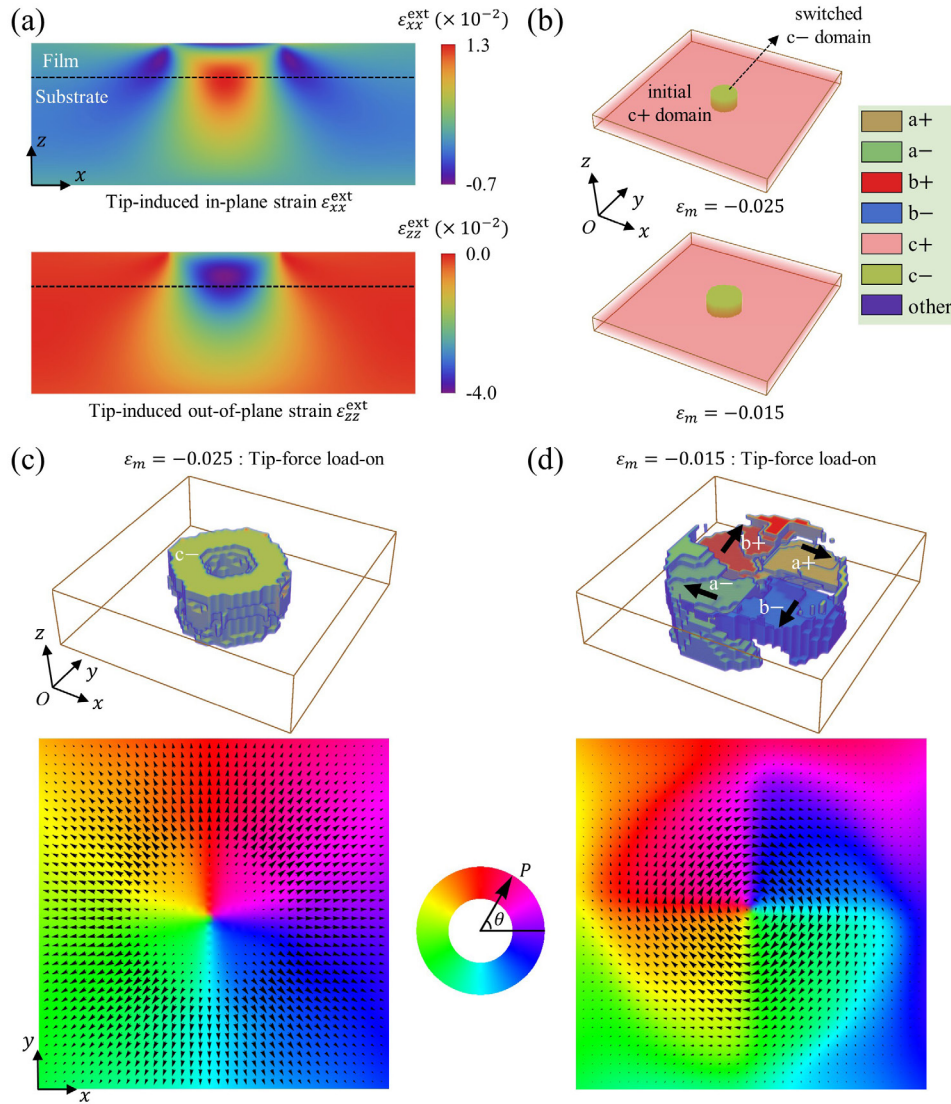


Figure 2. (a) Distribution of tip-force-induced strain $\epsilon_{xx}^{\text{ext}}$ and $\epsilon_{zz}^{\text{ext}}$ in the film/substrate system at the central x - z plane. (b) Dipole patterns when the tip-force is loaded off in BTO films under two different misfit strain, i.e. $\epsilon_m = -0.025$ and $\epsilon_m = -0.015$. (c) and (d) are the corresponding domain configurations of the two BTO films within the region (in size of $40\Delta \times 40\Delta \times 12\Delta$) near the tip when the tip-force is loaded on. The polarization vector maps projected on the x - y plane $z = 6\Delta$ are also presented, with the polarization directions being indicated by colors.

3. Results and discussions

3.1. Vortex formation under tip force and phase diagrams

To investigate the effect of tip-force on the domain structure in the BTO film, it is helpful to first gain an insight into the tip-force-induced strain distribution. Figure 2(a) depicts the distribution of in-plane strain $\epsilon_{xx}^{\text{ext}}$ and out-of-plane strain $\epsilon_{zz}^{\text{ext}}$ at the central x - z plane of the film induced by an external tip-force, with the pressing force of atomic force microscopy (AFM) tip being set to 1000 nN. One can see that for the film region right below the tip, $\epsilon_{xx}^{\text{ext}}$ changes from compression at the top surface to tension at the bottom interface along the film thickness; $\epsilon_{zz}^{\text{ext}}$ maintains compression across the film and its magnitude reaches maximum in the middle region of the film.

In the following, two 4.8 nm-thick BTO films under different misfit strains, i.e. $\epsilon_m = -0.025$ and -0.015 , are

considered. The simulation temperature is set to be 300 K, i.e. near the room temperature. At first, the films are initialized into a single domain state with an upward polarization; then the tip-force is exerted on the films and drives them to reach new equilibrium states; finally, with the tip-force loaded off, the films are relaxed to reach final steady states. Figure 2(b) depicts the domain patterns of the two films after the tip-force is loaded off. Here, we use the following notation of domain orientations: (i) the $a+$ domain, where $|\mathbf{P}| > 0.1$ (in unit of $P_0 = 0.26 \text{ C m}^{-2}$), $P_x > 0$ and $|P_x|/|\mathbf{P}| > 0.8$; (ii) the $a-$ domain, where $|\mathbf{P}| > 0.1$, $P_x < 0$ and $|P_x|/|\mathbf{P}| > 0.8$; (iii) the $b+$ domain, where $|\mathbf{P}| > 0.1$, $P_y > 0$ and $|P_y|/|\mathbf{P}| > 0.8$; (iv) the $b-$ domain, where $|\mathbf{P}| > 0.1$, $P_y < 0$ and $|P_y|/|\mathbf{P}| > 0.8$; (v) the $c+$ domain, where $|\mathbf{P}| > 0.1$, $P_z > 0$ and $|P_z|/|\mathbf{P}| > 0.8$; (vi) the $c-$ domain, where $|\mathbf{P}| > 0.1$, $P_z < 0$ and $|P_z|/|\mathbf{P}| > 0.8$; the remaining domains are denoted as ‘other’. It can be seen that for both films, the initial $c+$ domain region

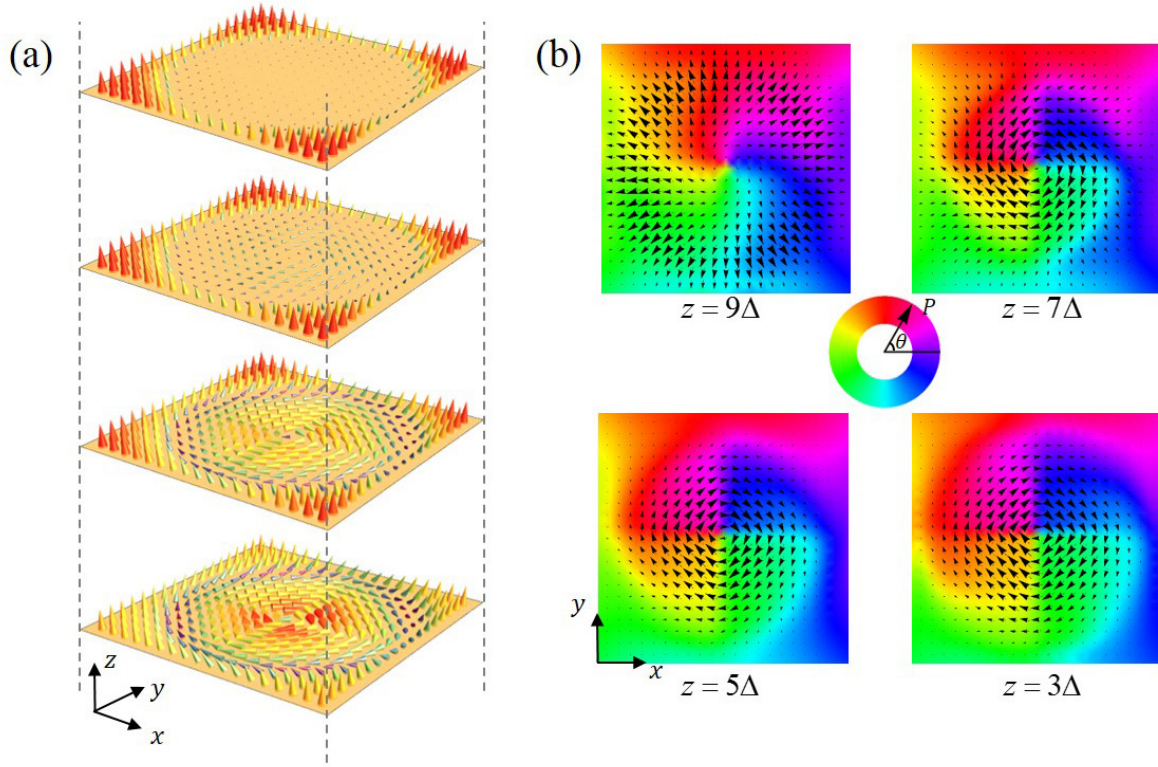


Figure 3. (a) 3D dipole configurations at different x - y planes of a 4.8 nm BTO film under a tip-force of 1000 nN at 300 K and a misfit strain $\varepsilon_m = -0.015$. (b) Corresponding 2D polarization vector maps at different x - y planes.

right below the tip is finally switched into $c-$ domain after the tip load-on and load-off process, which corresponds to the reported mechanical switching phenomenon [28]. Moreover, the switched domain of the film at $\varepsilon_m = -0.015$ has a larger lateral size than that of the film at $\varepsilon_m = -0.025$, which agrees with the experimental work [29].

The domain patterns of the films when the tip-force is loaded on are noteworthy. To see it more clearly, in figures 2(c) and (d) we depict the domain configuration of the two films within the region (in size of $40\Delta \times 40\Delta \times 12\Delta$) near the tip, respectively. Here, to have a clear illustration of domain profile, the ambient ‘ $c+$ ’ domain and the ‘other’ domain is set to be transparent. The polarization vector maps projected on the x - y plane $z = 6\Delta$ are also presented, with the polarization directions being indicated by colors. It shows that, for the film at $\varepsilon_m = -0.025$, a ‘ $c-$ ’ domain ring is induced near the edges of tip-film contact area. The region surrounded by the ‘ $c-$ ’ domain ring is actually the transparent ‘other’ domain, which shows a small magnitude of polarization $|\mathbf{P}| < 0.1$. On the x - y plane, the dipoles of the whole region present a divergent configuration, as also speculated in the previous work [37]. It should be noted also that, in this case, magnitude of the in-plane polarization at the exterior margin of tip-film contact area is relatively small (usually 0.1–0.2, see supplementary figure S2(a)) compared with the dominant out-of-plane polarization component P_z . Such a domain pattern is quite different from that of the film under a smaller compressive misfit strain, i.e. $\varepsilon_m = -0.015$.

For the latter case, as shown in figure 2(d), the polarization field beneath the tip exhibits rather large in-plane components,

especially near the bottom interface of the film. Remarkably, a closed domain flux with ordered ‘ $a+$ ’, ‘ $b-$ ’, ‘ $a-$ ’ and ‘ $b+$ ’ domains is formed (actually, among these domains there are domains has comparable P_x and P_y magnitude). This clearly indicates the formation of a ferroelectric vortex. Indeed, the polarization vectors on the x - y plane $z = 6\Delta$ exhibits a distinct vortex structure. In this film, the polarization vectors mainly lie in the x - y plane, with the in-plane components (usually >0.7) dominated over the out-of-plane component (supplementary figure S2(b)). Furthermore, while the polarization vectors of each x - y plane of the film form a regular vortex-like pattern, the exact dipole pattern is not uniform along the film thickness as shown in figure 3. When the plane is closer to the top surface of the film, the vortex dipole pattern is mixed with circular and divergent feature. The circular feature becomes more significant when it is closer to the bottom part of the film. Therefore, the whole 3D vortex pattern is complicated, which is obviously due to the large strain inhomogeneity inside the film induced by tip-force.

The mechanism of the tip-force-induced vortex can be explained as follows. Firstly, the external tip-force leads to large in-plane tensile strains, i.e. $\varepsilon_{xx}^{\text{ext}}$ and $\varepsilon_{yy}^{\text{ext}}$, and a large out-of-plane compressive strain $\varepsilon_{zz}^{\text{ext}}$, especially at the middle and bottom part of film (figure 2(a)). For the film under a small compressive misfit strain $\varepsilon_m = -0.015$, the external in-plane tensile strains and the out-of-plane compressive strain induce large in-plane polarization components, i.e. $P_{\text{in}} = \sqrt{P_x^2 + P_y^2}$, and at the same time, the out-of-plane polarization component is largely depressed. Secondly,

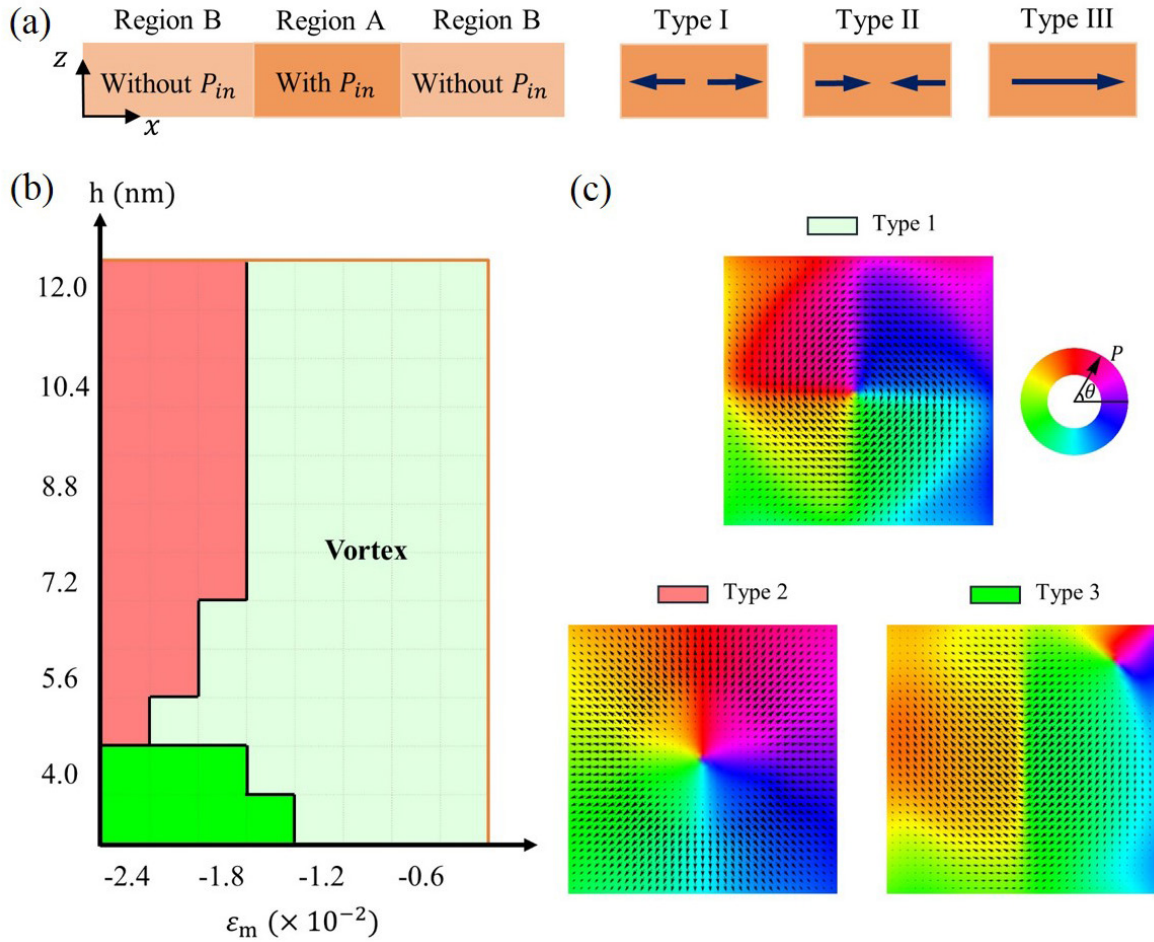


Figure 4. (a) Schematic illustration of the pattern formation in x - z plane of the BTO film. Four possible patterns in region ‘A’ where the polarization vectors have a large in-plane component beneath the tip are depicted. (b) Film thickness h versus misfit strain ϵ_m phase-diagram of the tip-induced vortex in BTO films under a fixed tip force of 1000 nN at 300 K. (c) Corresponding dipole configurations of the colored regions in (b).

although the tip-force is symmetric with respect to the tip axis, symmetric in-plane polarization distributions, i.e. head-to-head and tail-to-tail dipoles (type I and II in figure 4(a)), are not energetically favored for large P_{in} due to the large electrostatic energy, which makes the divergent or convergent dipole configurations unstable. Thus the projection of dipoles on x - z plane tends to align along the same direction (type III and IV in figure 4(a)) and results in the symmetry-breaking. Thirdly, due to the effect of tip-force is highly localized, the P_{in} is only induced in a small region (marked as region ‘A’ in figure 4(a)) beneath the tip, which is surrounded by the region without P_{in} (region ‘B’). From the perspective of in-plane directions, region ‘B’ provides poor charge screening conditions to region ‘A’, leading to the relatively open-circuit electrical boundary conditions of region ‘A’. In such a localized region, the large symmetry-broken P_{in} thus forms the vortex state under depolarization effect, similar to the mechanism of vortex formation in nanodot system. On the contrary, for case of large compressive misfit strain, e.g. $\epsilon_m = -0.025$, the total in-plane strain is not tensile enough to induce obvious P_{in} , therefore the depolarization effect is very weak and the symmetric divergent dipoles with small magnitude can be stable.

We further calculate the film thickness h versus misfit strain ϵ_m phase diagram of the tip-induced vortex, with the film thickness varying from 3.2 nm to 12 nm and misfit strain varying from -0.024 to -0.003 . As shown in figures 4(b) and (c), the BTO films can form three types of in-plane dipole pattern under the effect of the tip force. The type 1 and type 2 patterns denote the above-mentioned circular vortex pattern and divergent pattern, respectively. For type 3 pattern, the dipole pattern is noncentrosymmetric with respect to the tip axis and possesses a 90° domain pair as shown in figure 4(c) or a dominant polar domain (see supplementary figure S3). These three types of dipole pattern clearly show that the dipole distribution can be either symmetric or asymmetric around the tip axis. Note, the phase diagram is plotted according to the dipole configurations at the layers of the film near the bottom part of film. In fact, type 2 pattern is found to appear near the top surface of film for most cases. In figure 4(b), one can see that the circular vortex pattern forms at small compressive misfit strain for all film thicknesses and occupies a large area in phase diagram. At large compressive misfit strain, type 2 pattern is favored in thick films whereas type 3 pattern is favored in thin films. This phase diagram clearly shows that the tip-induced formation of vortex pattern is mainly affected by the

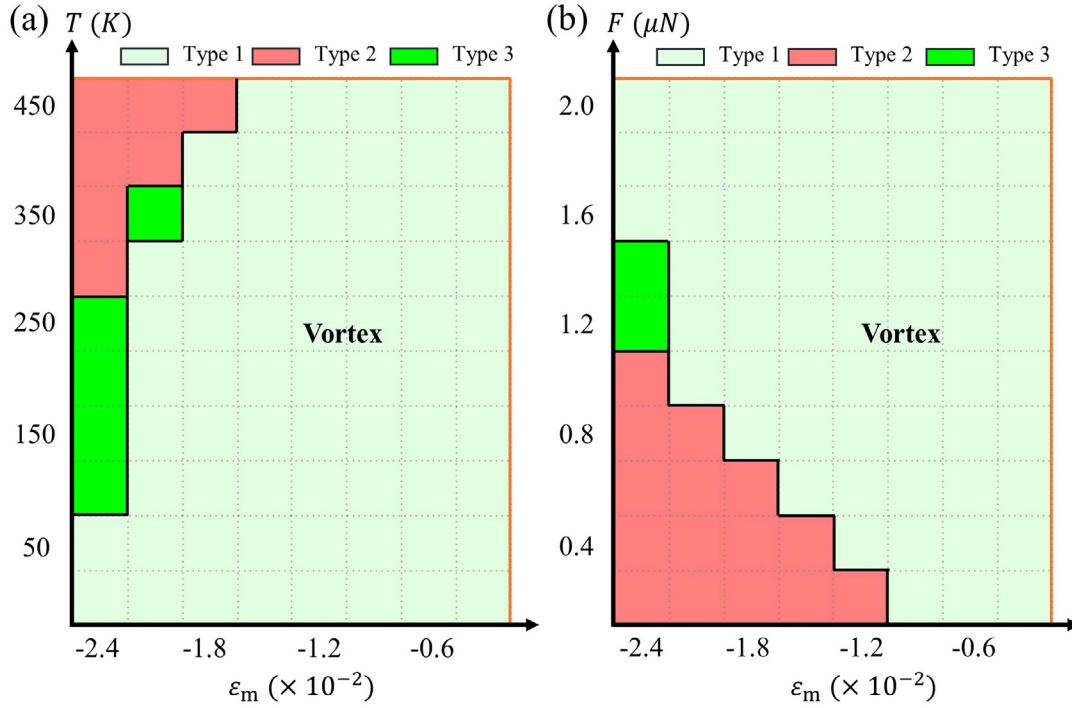


Figure 5. (a) Temperature T versus misfit strain ϵ_m phase-diagram of the tip-induced vortex in 4.8 nm-thick BTO films under a fixed tip force of 1000 nN. (b) Tip-force F versus misfit strain ϵ_m phase-diagram of the tip-induced vortex in 4.8 nm-thick BTO films at 300 K.

misfit strain rather than the film thickness, consistent with the formation scenarios previously discussed. The formation of type 3 pattern can be considered as an intermediate scenario between those of type 1 and type 2 patterns. For thin films at large compressive misfit strain and under tip loads, a moderate P_{in} is induced, with magnitude between those of type 1 and type 2, e.g. $0.1 < P_{in} < 0.6$ (see supplementary figure S3). It is large enough to result in an instability of divergent pattern (type 2). However, the lateral depolarization effect due to the surrounding domains in thin films is not strong as that in thick films. To avoid the large gradient energy of circular vortex pattern (type 1), the type 3 pattern with a dominant polar domain or domain pair is more energetically favored. The three different types of tip-force-induced dipole patterns clearly show that the polarization state of ferroelectric thin film under tip-force is much more complicated than what have been reported so far in the literature.

The temperature T versus misfit strain ϵ_m phase diagram of tip-induced vortex is shown in figure 5(a). Here the BTO films are 4.8 nm thick and the tip force is fixed to be 1000 nN. It can be seen that circular vortex emerges at most cases, especially at small misfit strain and low temperature. It is noteworthy that the circular vortex pattern is favored even at $\epsilon_m = -0.024$ when the temperature is lower than 50 K. This is attributed to the Landau energy, which tends to enlarge polarization (and thus P_{in}) at lower temperature to form vortex. When the temperature is higher at $\epsilon_m = -0.024$, P_{in} decreases and type 3 pattern appears. At even higher temperature, P_{in} is small enough and the symmetric divergent pattern (type 2) is favored. Figure 5(b) depicts the tip-force F versus misfit strain ϵ_m phase diagram of tip-induced vortex. Again, circular vortex pattern (type 1) is favored in most of the investigated conditions.

For large compressive misfit strain, e.g. $\epsilon_m = -0.024$, with the increase of tip-force, the favored dipole pattern changes from type 2, type 3 to type 1. This arises from the different P_{in} under different tip-forces. In general, the dipole patterns under external tip loads is directly driven by the elastic energy and is further determined by the competition between electrostatic energy (which favors circular vortex pattern) and gradient energy (which favors polar domain). For films subjected to small misfit strain, low temperature or large force, large P_{in} can be induced, and the electrostatic energy plays a dominant role, leading to the formation of circular vortex pattern. On the contrary, the divergent pattern is more favored in films subjected to conditions that induce small in-plane polarization. Under intermediate conditions, type 3 pattern with a dominant polar domain or domain pair may form.

3.2. The interaction between tip-induced vortices

It is interesting to further explore the interaction between two tip-induced vortices, especially the possible coupling between their chirality. A bigger simulation box, i.e. a mesh grid of $128\Delta \times 128\Delta \times 12\Delta$ with the grid space Δ being 1 nm, is employed in the following simulations. The distance d between the two tips varies from 48 nm to 4 nm. The loading force of each tip is 1000 nN. The misfit strain is set to be $\epsilon_m = -0.009$ to ensure the presence of vortex state. The dipole configurations in the x - y plane $z = 6\Delta$ for cases with different tip distances are illustrated in figure 6(a), with the area near the tips (in size of $50 \text{ nm} \times 16 \text{ nm}$) is depicted for clarity. Our result shows that for the tip distance $d \geq 24 \text{ nm}$, the two vortices are isolated and they can possess either the same (e.g. as figure 6(a) shows, both possess '0' state with anticlockwise

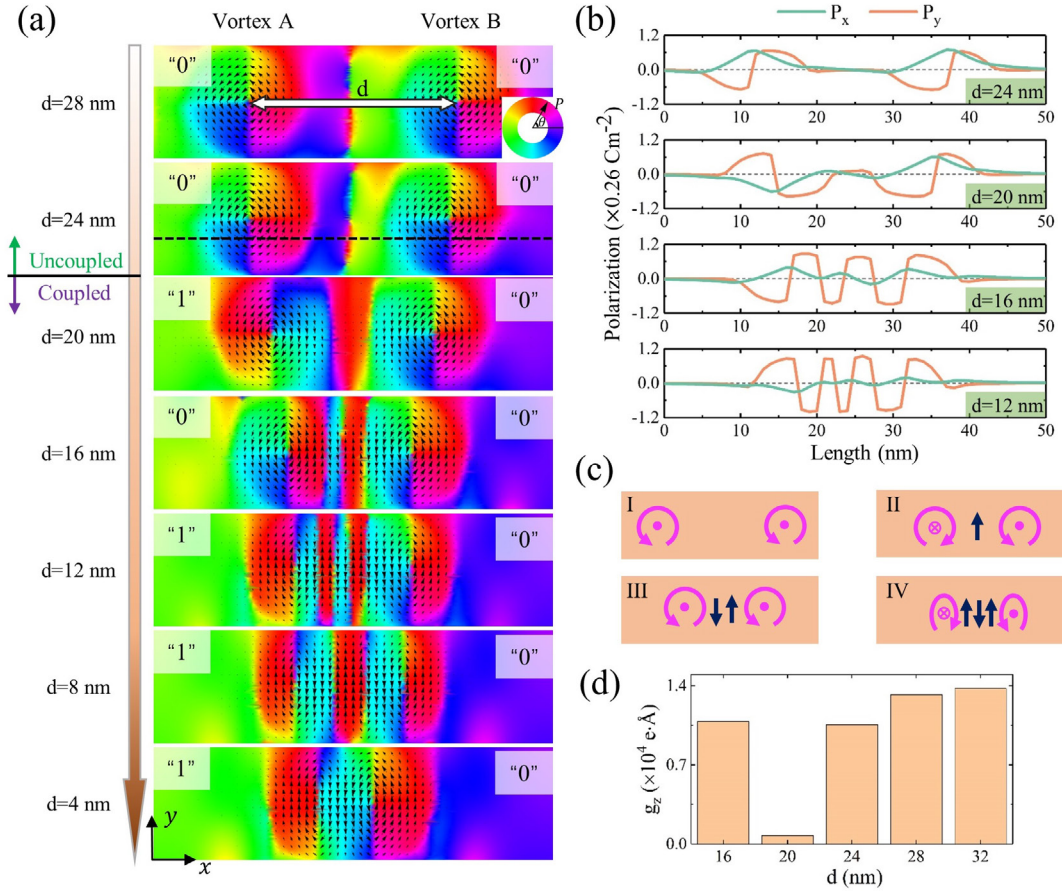


Figure 6. (a) In-plane dipole configurations in the x - y plane $z = 6\Delta$ of BTO films under two tip forces with different tip distances. Here, ‘0’ represents anticlockwise chirality of vortex and ‘1’ represents clockwise. The area near the tips (in size of $50 \text{ nm} \times 16 \text{ nm}$) is depicted for clarity. (b) In-plane polarization components P_x and P_y along the marked crossline (see (a) for $d = 24 \text{ nm}$) for the cases $d = 24 \text{ nm}$, 20 nm , 16 nm and 12 nm . (c) A schematic illustrating the mechanism of chirality coupling between two tip-induced vortices. (d) The toroidal moment of the two vortices in the $z = 6\Delta$ plane at different tip distances.

chirality) or opposite chirality (i.e. one in ‘0’ state and the other in ‘1’ state with clockwise chirality, not depicted here). However, the scenario is quite different for cases of small tip distances, where the two vortices are close enough to interact with each other and their chirality coupling is deterministic. For case of $d = 20 \text{ nm}$, the two vortices are always found to possess opposite chirality. When the tip distance decreases to $d = 16 \text{ nm}$, the chirality of the two vortices becomes identical again. When the tip distance $d \leq 12 \text{ nm}$, their chirality turns to be opposite again and remains unchanged. The critical tip distance $d = 24 \text{ nm}$ to keep two vortices isolated indicates that the maximum data storage density of isolated in-plane vortices in ferroelectric thin film is about 1 Tb in^{-2} . This is much lower than that previously estimated based on ferroelectric nanodisks [8].

To better understand the underlying mechanism of vortex chirality coupling, the in-plane polarization components P_x and P_y along the marked crossline (see figure 6(a) for $d = 24 \text{ nm}$) are depicted in figure 6(b) for the cases $d = 24 \text{ nm}$, 20 nm , 16 nm and 12 nm . The chirality relation of the vortices can be readily inferred from the polarization profiles nearby the vortices. For example, the chirality of the two vortices with the same (opposite) chirality must have P_x peaks in the same

(opposite) sign. Moreover, the vortex coupling is also reflected by nonzero polarization profile in the region between the two vortices. Obviously, both P_x and P_y in the middle region of the two vortices are zero at $d = 24 \text{ nm}$, as the two vortices are isolated. At $d = 20 \text{ nm}$, a small positive P_y appears in the middle region. With the decrease of tip distance, the magnitude of P_y increases in the middle region. Furthermore, at $d \leq 16 \text{ nm}$, the P_y curve in the middle region further shows alternating plateaus, indicating the formation of 180° domains. The presence of P_y in the middle region between the two tips arises from two reasons. Firstly, the in-plane strain $\varepsilon_{xx}^{\text{ext}}$ induced by tip-force in the middle region becomes more compressive and $\varepsilon_{yy}^{\text{ext}}$ becomes more tensile when the tip distance decreases (see Supplementary figure S4), which favors a larger P_y at smaller tip distance. Secondly, as the two vortices approach to each other, there would be a large polarization inhomogeneity (and consequently, a large depolarization field) in the middle region unless 180° domains nucleate to decrease the depolarization field. At $d = 24 \text{ nm}$ and 20 nm , both the in-plane strain and the depolarization effect in the middle region is small, thus P_y is near zero. At $d = 16 \text{ nm}$, the induced P_y is large and the depolarization effect due to the poor screening of region ‘B’ is strong, leading to the formation of 180° domains in the

middle region. At $d = 12$ nm, the middle region exhibits more 180° domains due to the even larger in-plane strain and depolarization effect.

In fact, it is the polarization pattern in the middle region between the two vortices that determines the coupling of vortex chirality. At a given tip loading force, the in-plane polarization pattern in the middle region strongly depends on the distance of the two tips. As schematically shown in figure 6(c), when there is no in-plane polarization induced in the middle region, the two vortices are not coupled, corresponding to the case $d \geq 24$ nm (case I). When the two tips are close enough, in-plane polarization appears in the middle region. As mentioned above, the compressive in-plane strain $\varepsilon_{xx}^{\text{ext}}$ together with the depolarization effect drive the in-plane polarization of the middle region to form a 180° domain pattern. The number of 180° domains in the middle region depends on the tip distance. Moreover, also to reduce the depolarization energy, the polarization of the two vortices and the 180° domain pattern must be in a flux-closure form. Therefore, if the polarization in the middle region forms a 180° domain pattern with odd number of domains, the chirality of the two vortices would be opposite. This corresponds to the case II of $d = 20$ nm with a single domain in the middle region and case IV of $d = 12$ nm with three domains in the middle region. On the contrary, if the 180° domain pattern is with even number of domains, the chirality of the two vortices would be identical. This corresponds to the case II of $d = 16$ nm, where the 180° domain pattern in the middle region has two domains, and the two vortices thus have the same chirality (figure R2). It should also be noted from figures 6(a) and (b) that as the tip distance decreases, the two vortices are gradually deformed into oblate shape, with a decrease of the P_x value and an increase of the P_y value. Figure 6(d) shows the toroidal moment of the two vortices in the $z = 6\Delta$ plane ($g_z = \iint_S [x \cdot (P_y - \overline{P}_y) - y \cdot (P_x - \overline{P}_x)] dS$, where \overline{P}_x and \overline{P}_y are the average value of P_x and P_y respectively) at different tip distances ($d > 12$ nm). One can see that the g_z value also clearly reflects the different couplings of vortex chirality at $d = 20$ nm and $d = 16$ nm.

4. Conclusion

In conclusion, based on 3D phase field simulations, we demonstrate a mechanical approach to induce isolated or interacting in-plane dipole vortices in ferroelectric films by pressing an AFM-tip. The formation of such dipole vortices is caused by a conjoint effect of the tip-force-induced depolarization effect and in-plane strain. Phase diagrams of the dipole pattern formation under tip loads are summarized based on a systematical study on influencing factors including film thickness, misfit strain, temperature and tip-force. It shows that vortex state is favored at a large spectrum of conditions, especially at small compressive misfit strain, low temperature and large tip-force. The existence of different types of tip-force-induced dipole patterns indicates that the polarization state of ferroelectric thin film under tip-force is much more complicated than what have been reported so far in the literature. The interaction

between two tip-induced vortices are also studied. The results indicate that, if the two tips are far away from each other, the two vortices are isolated; while if the two tips are closer than a critical distance, they are coupled in a deterministic way and their chirality is either identical or opposite, depending on the distance between the tips. A maximum data storage density of isolated in-plane vortices in ferroelectric thin film is estimated to be ~ 1 Tb in $^{-2}$.

The feasibility of mechanical writing in-plane dipole vortices by a tip-force and the deterministic chirality coupling of vortices as a function of tip distance should not be limited to BTO films. However, it must be pointed out that a shortcoming of the current strategy of mechanical writing in-plane dipole vortices is that the dipole vortices would not maintain stable once the tip-force is removed. One possible scheme to obtain stable vortices without tip force is to introduce a built-in strain inhomogeneity to the system, e.g. the one is caused by the structural inhomogeneity as examined by our additional simulation (see, supplementary figure S5). Another possibility might reside in materials with a small domain wall energy. Note, flexoelectricity is not a deterministic effect on the stability and interactions of the vortices. In comparison with the strain effect which induces the in-plane polarization and the depolarization effect that drives the in-plane polarization into flux-closure vortex, flexoelectricity is found to only slightly affect the vortex structure, mainly on the out-of-plane polarization. Considering the difference between three types of tip-force-induced dipole patterns, the vortex formation might be inferred from the abrupt change of the local tunnel conductance of the film in response to the influencing factors like tip force and temperature. In addition, whether the tip-force can lead to the formation of other chiral polar structures, for example, skyrmion in ferroelectric/magnetic heterostructures [38], is an interesting issue.

Acknowledgments

This work was supported by NSFC (Nos. 11602310, 11672339, 11832019, 11472313), and the Fundamental Research Funds for the Central Universities. Y Zheng also thanks support from Guangdong Natural Science Funds for Distinguished Young Scholar and China Scholarship Council.

ORCID iDs

W J Chen  <https://orcid.org/0000-0002-9276-7369>

References

- [1] Scott J F 2007 *Science* **315** 954
- [2] Scott J F and Paz de Araujo C A 1989 *Science* **246** 1400
- [3] Catalan G, Seidel J, Ramesh R and Scott J F 2012 *Rev. Mod. Phys.* **84** 119
- [4] Choi T, Lee S, Choi Y J, Kiryukhin V and Cheong S W 2009 *Science* **324** 63
- [5] Mathews S, Ramesh R, Venkatesan T and Benedetto J 1997 *Science* **276** 238

- [6] Garcia V, Fusil S, Bouzehouane K, Enouz-Vedrenne S, Mathur N D, Barthélémy A and Bibes M 2009 *Nature* **460** 81
- [7] Ahn C H, Rabe K M and Triscone J M 2004 *Science* **303** 488
- [8] Naumov I I, Bellaiche L and Fu H 2004 *Nature* **432** 737
- [9] Zheng Y and Chen W J 2017 *Rep. Prog. Phys.* **80** 086501
- [10] Yadav A K 2016 *Nature* **530** 198
- [11] Das S, Ghosh A, McCarter M R, Hsu S-L, Tang Y-L, Damodaran A R, Ramesh R and Martin L W 2018 *APL Mater.* **6** 100901
- [12] Geng W et al 2018 *ACS Nano* **12** 11098
- [13] Rodriguez B J, Gao X S, Liu L F, Naumov I I, Bratkovsky A M, Hesse D and Alexe M A 2009 *Nano Lett.* **9** 1127
- [14] Gruverman A, Wu D, Fan H F, Vrejoiu I, Alexe M, Harrison R J and Scott J F 2008 *J. Phys.: Condens. Matter* **20** 342201
- [15] Naumov I I and Fu H 2008 *Phys. Rev. Lett.* **101** 197601
- [16] Chen W J and Zheng Y 2015 *Acta. Mater.* **88** 41
- [17] Ma L L, Ji Y, Chen W J, Liu J Y, Liu Y L, Wang B and Zheng Y 2018 *Acta Mater.* **158** 23
- [18] Yuan S, Chen W J, Ma L L, Ji Y, Xiong W M, Liu J Y, Liu Y L, Wang B and Zheng Y 2018 *Acta Mater.* **148** 330
- [19] Liu J, Ji Y, Yuan S, Ding L, Chen W and Zheng Y 2018 *NPJ Comput. Mater.* **4** 78
- [20] Chen W J, Zheng Y and Wang B 2012 *Appl. Phys. Lett.* **100** 062901
- [21] Prosandeev S, Ponomareva I, Kornev I and Bellaiche L 2008 *Phys. Rev. Lett.* **100** 047201
- [22] Lich L V, Shimada T, Wang J, Dinh V H, Bui T Q and Kitamura T 2017 *Phys. Rev. B* **96** 134119
- [23] Chen W J, Zheng Y, Wang B and Liu J Y 2014 *J. Appl. Phys.* **115** 214106
- [24] Balke N et al 2012 *Nat. Phys.* **8** 81
- [25] Yadav A K et al 2019 *Nature* **565** 468
- [26] Li Y et al 2017 *NPJ Quantum Mater.* **2** 43
- [27] Kim J, You M, Kim K E, Chu K and Yang C H 2019 *NPJ Quantum Mater.* **4** 29
- [28] Lu H, Bark C W, De Los Ojos D E, Alcala J, Eom C B, Catalan G and Gruverman A 2012 *Science* **336** 59–61
- [29] Wen Z, Qiu X, Li C, Zheng C, Ge X, Li A and Wu D 2014 *Appl. Phys. Lett.* **104** 042907
- [30] Chen W J, Liu J, Ma L, Liu L, Jiang G L and Zheng Y 2018 *J. Mech. Phys. Solids* **111** 43
- [31] Shi Y and Wang J 2018 *Phys. Rev. B* **97** 224428
- [32] Yudin P V and Tagantsev A K 2013 *Nanotechnology* **24** 432001
- [33] Yurkov A S and Tagantsev A K 2016 *Appl. Phys. Lett.* **108** 022904
- [34] Li Y L, Cross L E and Chen L Q 2005 *J. Appl. Phys.* **98** 064101
- [35] Zheng Y and Woo C H 2009 *Appl. Phys. A* **97** 617
- [36] Kretschmer R and Binder K 1979 *Phys. Rev. B* **20** 1065
- [37] Cao Y, Morozovska A and Kalinin S V 2017 *Phys. Rev. B* **96** 184109
- [38] Wang L et al 2018 *Nat. Mater.* **17** 1087